A method for density fluctuation measurements using pulse reflectometry

O. Krutkin, S. Brunner, S. Coda

École Polytechnique Fédérale de Lausanne (EPFL), Swiss Plasma Center (SPC), CH-1015 Lausanne, Switzerland

E-mail: oleg.krutkin@epfl.ch

January 2023

Abstract. An analytical 1D model based on the WKB approximation is used to study the properties of a short pulse reflectometry diagnostic in a magnetic fusion device. Expressions linking the pulse delay with the parameters of the turbulence near the cut-off layer are derived for both ordinary and extraordinary polarizations of the probing beam. These results are used to develop a method for measuring the turbulence amplitude and the radial correlation length. The analytical conclusions and the proposed method are validated using full-wave numerical modelling. The latter is also used to study the limitations of the method and potential experimental effects not included in the reduced model.

1. Introduction

Active microwave methods, such as interferometry and reflectometry, are commonly used for routine measurements of the electron density profile in magnetized plasmas [1]. Due to the fact that the probing beam propagation is affected by turbulent density perturbations, various techniques have been developed for reflectometry to measure the characteristics of the plasma turbulence.

One of the first approaches to turbulence measurements was the fluctuation reflectometry diagnostic [2, 3], in which the plasma is probed at a fixed frequency under normal incidence with respect to the cut-off surface and the variation of the phase of the reflected signal is interpreted as the perturbation of the density profile at the cut-off. Using several probing frequencies, correlation techniques are used to obtain the radial correlation length of the turbulence [4, 5]. In the case of fast sweeping reflectometry (FSR), in which the probing frequency is swept throughout the discharge, the method for finding the amplitude of turbulent density fluctuations was developed [6, 7]. Additionally, utilizing oblique incidence of the probing beam with respect to the magnetic surface, the Doppler reflectometry diagnostic [8] provides information about the poloidal wavenumber spectrum of the turbulence as well as its rotation velocity,

while radial correlation Doppler reflectometry [9] provides improved measurements of the radial correlation length of the turbulence.

The radar pulse reflectometry technique was proposed and employed for density profile measurements [10].The diagnostic has the benefit of operating in the time-domain, making it possible to directly measure the delay of the reflected pulses and to separate them from parasitic reflections and scattering away from the cut-off.

Considerable experimental [11, 12, 13] and theoretical [14, 15] work was carried out to develop the diagnostic, most of it focused on density profile measurements rather than turbulence studies. Recently, a short-pulse reflectometry (SPR) system has been developed and employed on the TCV tokamak [16, 17]. It is capable of using short ($<$ ns) microwave probing pulses and digitally recording the envelope of the reflected pulse.

So far the SPR system at TCV has only been used for the fast reconstruction of the electron density profile. But similar to the FSR diagnostic, SPR measurements are affected by plasma turbulence and can potentially provide related information. An investigation into the implications of SPR's unique capability to digitally record the reflected pulse for turbulence studies has recently been carried out [18]. Unfortunately, it concludes that, in the current configuration of the SPR diagnostic, the pulse shape is not directly connected to the plasma turbulence parameters.

Within this paper, rather than focusing on the shape of the pulse, the possibility of using the statistical properties of the delay times measured by SPR to determine the properties of the plasma turbulence is explored. We present a novel method for measuring the turbulence amplitude and its radial correlation length utilizing the standard SPR configuration.

We will start by developing an analytical theory, presented in Sec. 2 and Appendix A. The results will then be validated using the CUWA [19] code in Sec. 3. CUWA is a full-wave code, which was used to produce pulse delays corresponding to a particular density perturbation while accounting for all the relevant physics. Detailed information about the code will also be given in Sec. 3. In Sec 4, the same code will be used to test the proposed method and its limitations that could play a role in experiments. An overview of the final method, a comparison with the currently available diagnostics as well as future prospects, is presented in Sec. 5. Lastly, the main points of the paper are summarized in the final concluding section.

2. Theoretical model

2.1. Analytical considerations

Within this work, we will limit ourselves to a simple 1D WKB interpretation of the probing pulse delays measured by SPR. We will start by considering ordinary (O) polarization of the probing wave and generalize the results later. Since the goal of the work is turbulence measurements, we will separate the instantaneous electron

density profile n into the stationary background density n_0 and its fluctuations δn. We will assume the background density profile to have a linear dependence on the radial coordinate (designated x) $n_0 = n_c \frac{x}{L}$. Here, $n_c = \frac{m_e \omega^2}{4\pi e^2}$ is the critical density, corresponding to the cut-off of the probing frequency ω. With this definition L is a frequency dependent quantity ($L(\omega) \propto \omega^2$), which represents both the cut-off coordinate and the density gradient scale length at the cut-off.

Within this work we will not consider the temporal characteristics of the turbulence. For that reason we will not make any specific assumption about the frequency spectrum of δn and will only assume that the density perturbation averages to zero ($\langle \delta n(x) \rangle = 0$). Under these assumptions, the pulse delay can be represented by the following integral:

$$t_d = 2\int_0^L \frac{dx}{v_g} = \frac{2}{c}\int_0^L \frac{dx}{\sqrt{1 - \frac{x}{L} - \frac{\delta n(x)}{n_c}}}, \tag{1}$$

where v_g stands for group velocity. The second equality comes from the specific dispersion relation for O-mode [20]. The main contribution to this integral comes from the vicinity of the cut-off $x = L$. Unfortunately, that is also the region where the WKB approximation breaks down and trying to apply the standard perturbation approach to account for the density fluctuations can result in a diverging integral [20]. Nevertheless, previous analytical work [21, 22] shows qualitatively correct results can still be obtained using the WKB approximation in the cut-off region.

To overcome the potential divergence of the integral, we shall assume that density fluctuations have a simple form that can be directly integrated. Specifically, we will assume that the density fluctuation at the cut-off can be represented by a step-like perturbation with its width dictated by the turbulence radial correlation length $2l_{cx}$. This simplified model will allow us to analytically integrate Eq. (1). While a more complex and realistic shape could be used, we have found this simplification to be sufficient to obtain correct qualitative results. As described later in this section, these results were then confirmed with numerical integration without relying on the step function simplification, allowing us to obtain the final quantitative expression. The geometry of the model is illustrated in Fig 1:

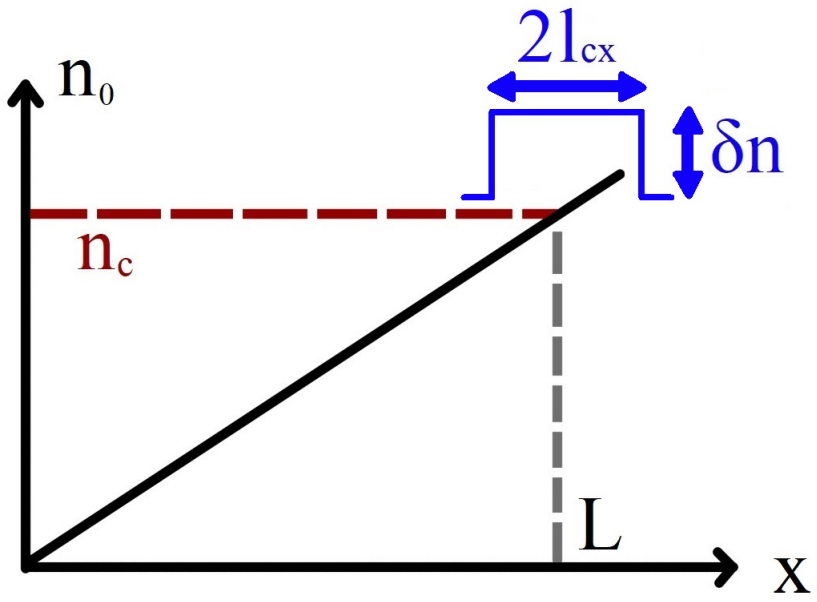

Figure 1. An illustration of the model geometry

The perturbation of the density results in a shift of the cut-off, the value of which depends on the amplitude dn.There are two principal cases one needs to consider. If the shift of the cut-off is small compared to l_{cx} (which corresponds to small amplitude of dn), then considering a single step-like density perturbation is enough to account for it. In this case, as illustrated by Fig. 2, the average shift of the cut-off is 0:

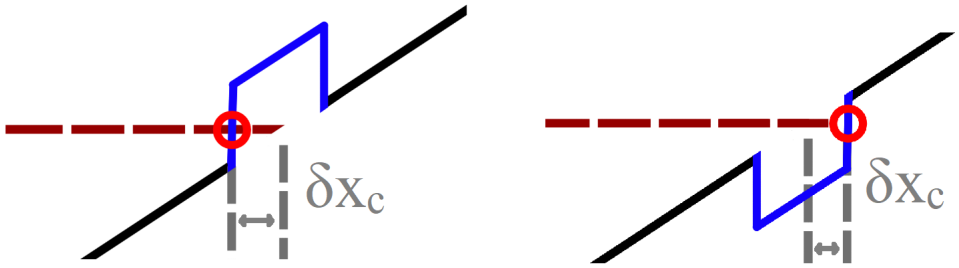

Figure 2. An illustration of symmetric cut-off shift

In the opposite case of large turbulence amplitudes, several density "steps" have to line up to move the cut-off inward and thus increase the delay. At the same time, a single density "step" can result in the cut-off moving significantly outwards and the delay time decreasing. In this situation, illustrated in Fig. 3, the average cut-off delay effectively will be reduced and considering a single density step-like perturbation at the cut-off is not sufficient to describe the perturbation of the delay time by a density fluctuation.

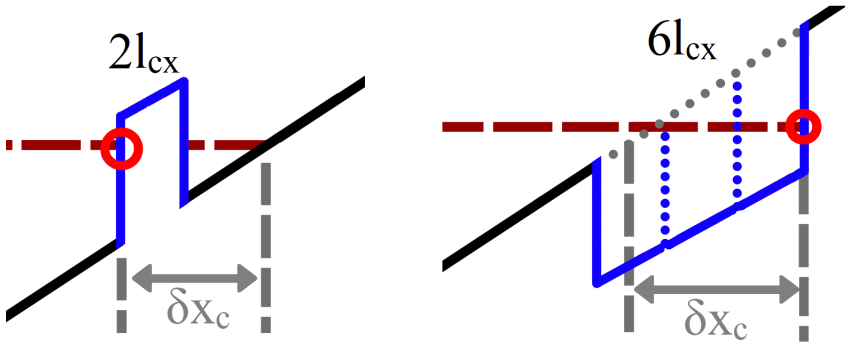

Figure 3. An illustration of asymmetric cut-off shifts

Within this work, we will focus on the small amplitude case, illustrated by Fig. 2. It is defined by the condition that the cut-off shift be smaller than the radial correlation length of the turbulence. In the case of ordinary polarization and linear profile of the background density, the position of the cut-off is expressed by Eq. (2):

$$n(x_c) = n_c = n_c\frac{x_c}{L} + \delta n(x_c), \tag{2}$$

$$\delta x_c = x_c - L = -\frac{\delta n}{n_c}L; \tag{3}$$

To obtain Eq. 3, we have assumed that the value of δn does not change between the original (L) and perturbed (x_c) cut-offs, as illustrated by Fig. 2. Equation (3) allows us to express the critical density amplitude δn_{crit}, for which the cut-off shift is equal to l_{cx}, as well as statistical properties of the cut-off shift:

$$\langle \delta x_c \rangle = 0; \tag{4}$$

$$\sqrt{\langle \delta x_c^2 \rangle} = \frac{\sqrt{\langle \delta n^2 \rangle}}{n_c}L; \tag{5}$$

$$\frac{\delta n_{crit}}{n_c} = \frac{l_{cx}}{L}; \tag{6}$$

From this point on, we will limit ourselves to considering the regime in which r.m.s.(δn) << δn_{crit}. Approximating the density perturbation by a single step-like function centered at the cut-off will allow us to integrate the reciprocal of the group velocity and obtain a relation for the pulse delay following Eq. 1:

$$t_d = \frac{2}{c}\int_0^L \frac{dx}{\sqrt{1-\frac{x}{L}-\frac{\delta n(x)}{n_c}}} = \frac{4L}{c} - \frac{4\sqrt{Ll_{cx}}}{c} + \frac{4\sqrt{L}\sqrt{l_{cx}-L\frac{\delta n}{n_c}}}{c} \tag{7}$$

Taking into account the condition r.m.s.(δn) << δn_{crit}, we can further simplify this expression:

$$t_d = \frac{4L}{c} - \frac{2L}{c}\sqrt{\frac{L}{l_{cx}}}\frac{\delta n}{n_c}, \tag{8}$$

$$\langle t_d \rangle = \frac{4L}{c}, \tag{9}$$

$$\sqrt{\langle (t_d - \langle t_d \rangle)^2 \rangle} = \frac{2L}{c}\sqrt{\frac{L}{l_{cx}}}\frac{\sqrt{\langle \delta n^2 \rangle}}{n_c}. \tag{10}$$

From this formula we can thus directly link the r.m.s. of SPR delays to the r.m.s. of the density fluctuations. However, to apply it, we need to have a prior knowledge of the radial correlation length of the turbulence. Such a measurement is usually done by employing the Radial Correlation Reflectometry (RCR) technique [4]. The technique is based on computing the Cross-Correlation Function (CCF) between the reflected signals corresponding to different probing frequencies. This CCF is then interpreted as the turbulence two-point correlation function between the cut-off positions.

Using SPR, we can apply a similar technique by measuring delays corresponding to neighboring probing frequencies and finding the correlation between these delays depending on the frequency separation. One point to note is that the length L is proportional to the square of the probing frequency ω within our model. We will select a central frequency ω_0 and designate the corresponding value of L as L_0. From Eqs. (8) - (10) one then obtains:

$$\delta t_d(\omega) = t_d(\omega) - \frac{4L(\omega)}{c} = -\frac{2L_0}{c}\sqrt{\frac{L_0}{l_{cx}}}\frac{\omega}{\omega_0}\frac{\delta n}{n_c(\omega_0)}, \tag{11}$$

$$\langle \delta t_d(\omega_0)\delta t_d(\omega)\rangle = \left(\frac{2L_0}{c}\right)^2 \frac{L_0}{l_{cx}}\frac{\omega}{\omega_0}\frac{\langle \delta n(x_c(\omega_0))\delta n(x_c(\omega))\rangle}{n_c(\omega_0)^2}. \tag{12}$$

Using this formula, we can represent the normalized CCF of the delay perturbations in terms of the normalized two-point CCF of the turbulence:

$$\mathrm{CCF}_{\delta t_d}(\omega, \omega_0) = \frac{\langle \delta t_d(\omega)\delta t_d(\omega_0)\rangle}{\sqrt{\langle \delta t_d(\omega_0)\delta t_d(\omega_0)\rangle \langle \delta t_d(\omega)\delta t_d(\omega)\rangle}} = \mathrm{CCF}_{\delta n}(x_c(\omega), x_c(\omega_0)). \tag{13}$$

Using Eqs. (10) and (13), one can obtain information about both radial correlation length and amplitude of the turbulent density perturbations from a set of SPR measurements at several close probing frequencies and the background density profile information needed to determine $x_c\omega$.

The same logic can be applied to X-mode probing, assuming background parameters in the vicinity of the cut-off do not change significantly. Given that the derivation for this case is rather cumbersome, it is given in Appendix A. The final formulas for the critical turbulence amplitude and delay r.m.s. in the case of X-mode are:

$$\frac{\delta n_{crit}}{n_0(x_c)} = 2\frac{l_{cx}}{L_c}\frac{\omega}{\omega_{pe}}\sqrt{1 + \frac{\omega_{ce}^2}{4\omega_{pe}^2}}, \tag{14}$$

$$\sqrt{\langle (t_d - \langle t_d \rangle)^2 \rangle} = \frac{L_c}{c}\sqrt{\frac{L_c}{l_{cx}}}h(x_c)\frac{\omega_{pe}}{\omega\sqrt{1+\frac{\omega_{ce}^2}{4\omega_{pe}^2}}}\frac{\sqrt{\langle \delta n^2 \rangle}}{n_0(x)}, \tag{15}$$

with $h(x)$ and L_c given by Eqs. (A.5) and (A.6).

Regarding the normalized CCF of the delay times, Eq. (13) applies for both modes.

Equations (10) and (15) rely on a number of simplifications. First of all, a linear background density profile (and magnetic field profile in the case of X-mode) does not describe realistic plasma conditions. This issue can be solved by treating the value L as the *gradient scale length* of the density profile at the cut-off. This generalization usually works for the analysis of reflectometry diagnostics [23, 24] and, given that we only consider the density fluctuations at the cut-off, should be all the more valid in our case.

Another simplification involves reducing the problem to 1D. However, analytical studies for RCR have previously shown that the results obtained in 1D [21] are in qualitative agreement with 2D considerations [23].

Finally, the simplification of only associating the perturbation of the delay time to the shift of the cut-off (and using the WKB approximation there) is also not rigorous, although it has been successfully utilized before for Doppler reflectometry [25]. While Eq. (1) implies that the density perturbations at the cut-off provide the dominant contribution to the integral, it is not obvious that one can actually neglect them everywhere else.

For all these reasons, to validate our analytic derivations, numerical modeling is necessary.

2.2. Numerical integration

First, to justify the assumption that the r.m.s. of δt_d is determined by the density fluctuations in the vicinity of the cut-off, a numerical integration of Eq. (1) was carried out. To this end, the integral along the entire beam propagation path was considered, including all corresponding density perturbations.

To produce a sample of the density fluctuations, a Gaussian spectrum with random phase was utilized:

$$\delta n\left(\kappa\right) \propto \exp\left(-\frac{\kappa^2 l_{cx}^2}{8} + i\Delta\phi(\kappa)\right). \tag{16}$$

Here, κ corresponds to the radial wavenumber of the density perturbation. A set of samples $\delta n(x)$ was obtained by performing the inverse Fourier transform of the spectrum (and retaining the real part), including a random phase $\Delta\phi(\kappa)$ sampled uniformly over $[0, 2\pi]$. Each sample was multiplied by a constant factor to have a specific r.m.s. value and then plugged into Eq. (1). A total of 3000 samples were used to guarantee convergence (no significant difference between 1000 and 3000 samples was found). Once a set of 3000 delay times for each density perturbation amplitude was obtained for a

linear n_0 profile, the delay r.m.s. was computed and compared to the prediction given by Eq. (10).

Since the density perturbations produced using the spectrum in Eq. (16) are uniform in amplitude, the value of relative amplitude $\delta n(x)/n_0(x)$ would actually increase towards the periphery of the plasma. This increase is in line with realistic plasma conditions in which turbulence is stronger closer to the plasma edge.

To avoid strong numerical reflection, in full-wave computations presented in later sections the total density profile at the very edge of the plasma was smoothed utilizing a Gaussian filter with a standard deviation equal to half the probing wavelength. An example of a typical normalised turbulence amplitude profile is given in Fig. 4.

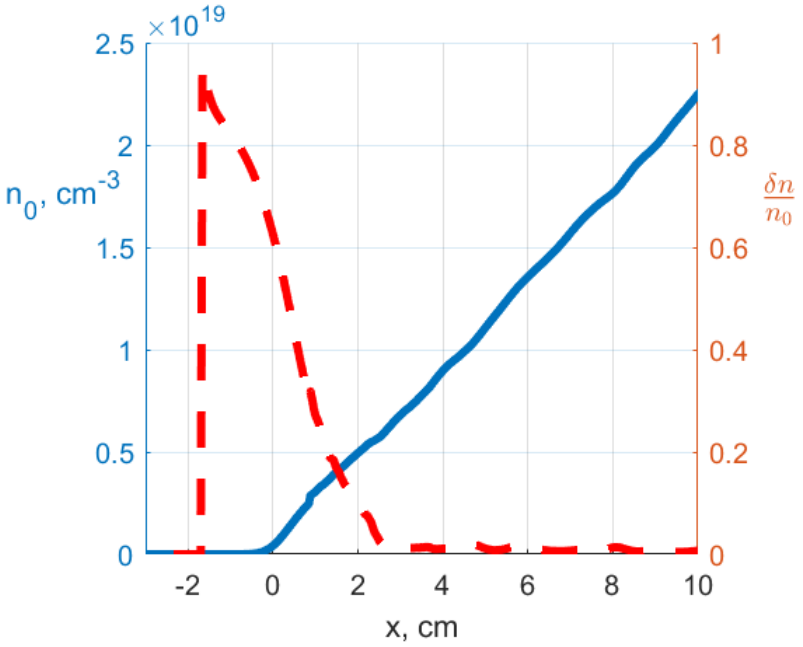

Figure 4. Typical normalised turbulence amplitude (in red on the right axis) and average density profile (in blue on the left axis) in the computation based on 1000 samples.

As can be seen from the figure, the level of turbulence increases towards the edge up to very large values. Another noticeable effect is that, even with 1000 samples, there are still noticeable statistical errors in the average density profile, which could partially explain discrepancies observed in the next Section.

Utilizing numerical integration, an example of the resulting dependence of the delay r.m.s. on the r.m.s. of density perturbations for the case of O-mode is given in Fig. 5.

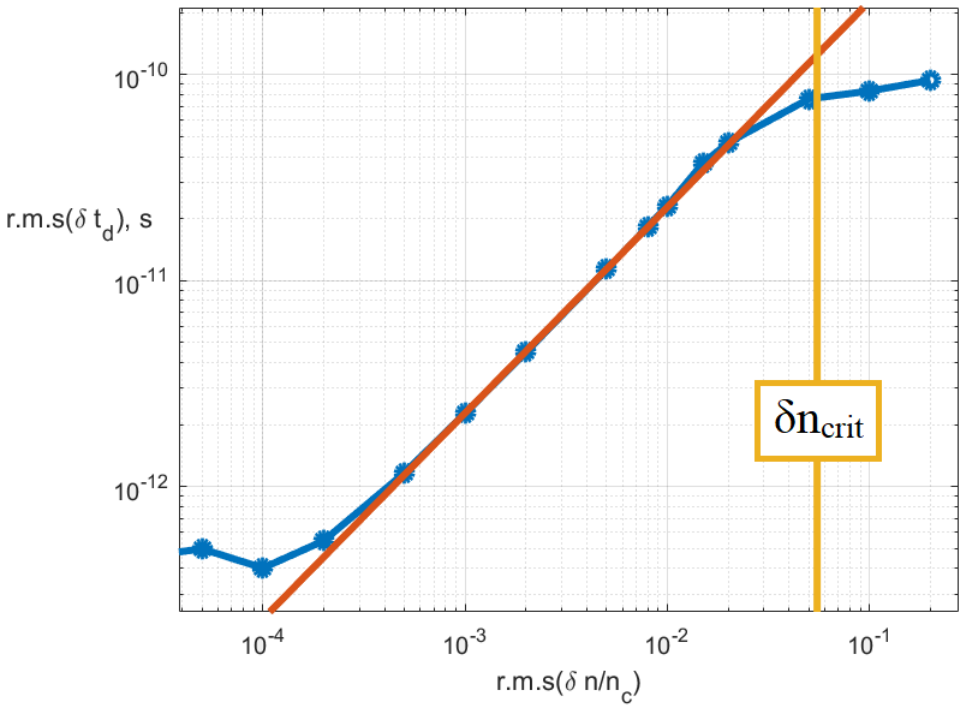

Figure 5. Numerical integration example for $L = 4$ cm and $l_{cx} = 0.22$ cm. R.m.s of O-mode time delay vs the amplitude of the turbulence. The blue curve corresponds to the numerical integration, the red line is the prediction given by Eq. (10), multiplied by 2. The yellow line is the threshold amplitude given by Eq. (6).

The points at low fluctuation amplitudes that deviate from theoretical expectations correspond to the delay r.m.s. becoming comparable to the numerical error in estimating Eq. (1), which results in overestimated values. These points can be ignored. It is important to note that in every case considered, within a wide range of parameters ($L_0 = 4{-}20$ cm, $l_{cx} = 0.01 = 1$ cm), the prediction given by Eq. (10) was exactly a factor of 2 smaller than the computation results. As the only difference between numerical and analytical models is the use of step-like density perturbations, we attribute this difference to that simplification. Since the numerical integration was using more realistic perturbations, we incorporate this ratio into our simplified formula, so that for further validation we will be using the modified expression:

$$\sqrt{\langle \delta t_d^2 \rangle} = \sqrt{\langle (t_d - \langle t_d \rangle)^2 \rangle} = \frac{\mathbf{4}L}{c} \sqrt{\frac{L}{l_{cx}}} \frac{\sqrt{\langle \delta n^2 \rangle}}{n_c}. \tag{17}$$

Next, the numerical integration was carried out for a set of 251 critical density values, each corresponding to a different probing frequency (using the same set of δn samples for each frequency), to compute the CCF of delays corresponding to different probing frequencies. An example of the integration result for a turbulence r.m.s. of $5 \cdot 10^{-3} n_c(\omega_0)$ is given in Fig. 6.

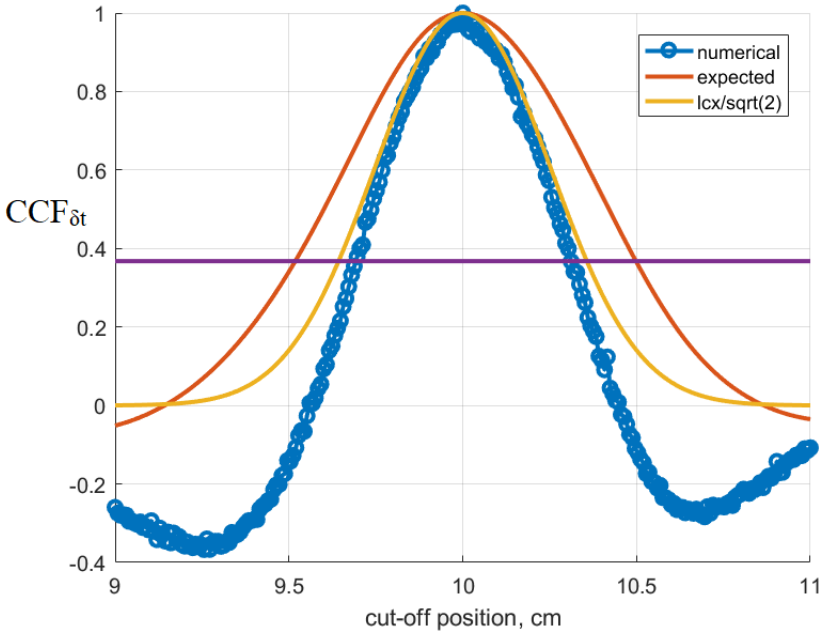

Figure 6. CCF of O-mode time delays corresponding to different cut-off positions for $L = 10$ cm and $l_{cx} = 0.5$ cm. The blue curve corresponds to the numerical integration, the red line is the prediction given by Eq. (13). The yellow line is the same formula with l_{cx} divided by $\sqrt{2}$. The purple line corresponds to $1/e$ level.

.

Once again, in a systematic scan over L_0 and l_{cx} we find that a rescaling of l_{cx} by a factor of $1/\sqrt{2}$ is necessary to obtain a more accurate value of the correlation length. This empirical correction would need to be tested further in future work, in particular for a non-Gaussian spectrum, which was shown to be significantly unrealistic in [26]. Nevertheless, Eq. (17) only has a weak dependence on l_{cx}, so an error in its measurement is acceptable.

Finally, a numerical integration for X-mode polarization was also carried out using the X-mode dispersion relation (Eq. (A.1)) to find the group velocity. An example of delay r.m.s. as a function of the density perturbation amplitude is presented in Fig. 7.

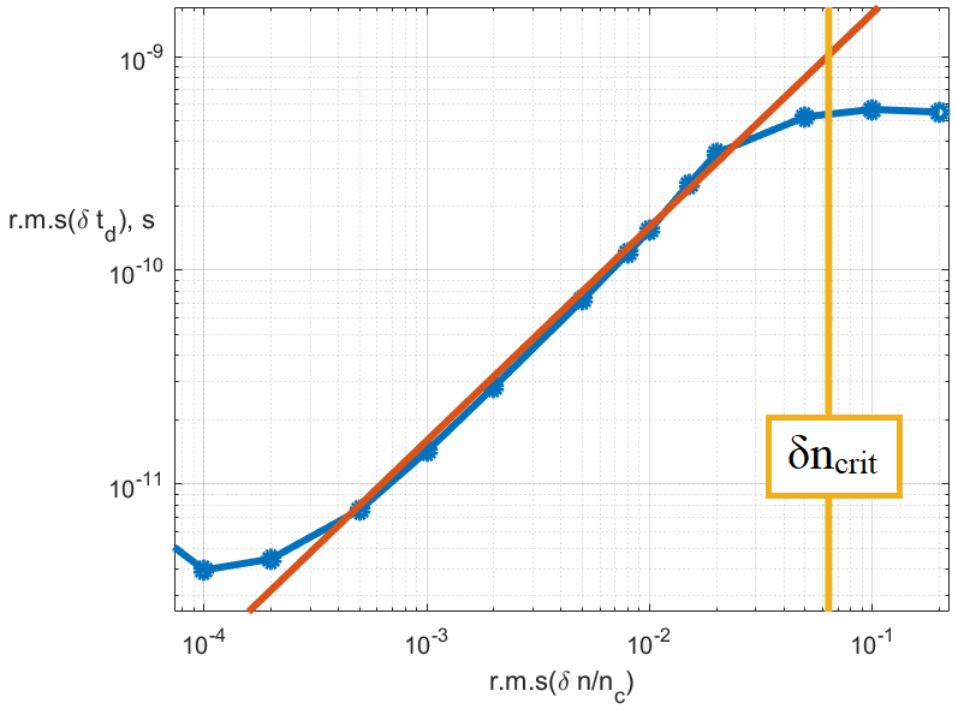

Figure 7. R.m.s of X-mode time delay vs amplitude of the turbulence for $L = 4$ cm and $l_{cx} = 0.5$ cm. The blue curve corresponds to the numerical integration, the red line is the prediction given by Eq. (15), multiplied by 2. The yellow line is the threshold amplitude given by Eq. (14).

Once again, a factor of 2 was empirically found between the analytical prediction given by Eq. (15) and numerical integration results. The consistency of this effect between O and X mode corroborates the explanation of it being an artifact of the step-like density perturbation approximation.

Numerical factors aside, the integration seems to confirm the approach of attributing the time delay r.m.s. to the density fluctuations at the cut-off.

3. Full-wave validation

3.1. Computational setup

To further validate Eqs. (10) and (17), full-wave modelling was carried out using the GPU-enabled code CUWA. CUWA is a finite difference time domain full-wave code in which the wave equation is solved within the cold plasma approximation. Further details about the specific implementation can be found in [19]. For the purpose of this work the code was adapted to have a pulsed microwave source rather than a continuous one. The computations were carried out on a 2D grid, using frozen density perturbations and a linear background density profile in slab geometry. The source term was adapted for pulsed operation and the signal was recorded throughout all timesteps to obtain the returning pulses.

Similarly to the previous section, a Gaussian turbulence spectrum (now two-dimensional) was used to produce random density perturbations:

$$\delta n\left(\kappa, q\right) \propto \exp\left(-\frac{\kappa^2 l_{cx}^2}{8} - \frac{q^2 l_{cy}^2}{8} + i\Delta\phi(\kappa, q)\right). \tag{18}$$

Here, q corresponds to the poloidal wavenumber of the density perturbation, while *kappa* still represents the radial wavenumber. The set of delay times in this case was obtained by computing over 1000 random samples. An example of a CUWA computation ($L_0 = 20$ cm, $l_{cx} = l_{cy} = 1$ cm) is given in Fig. 8.

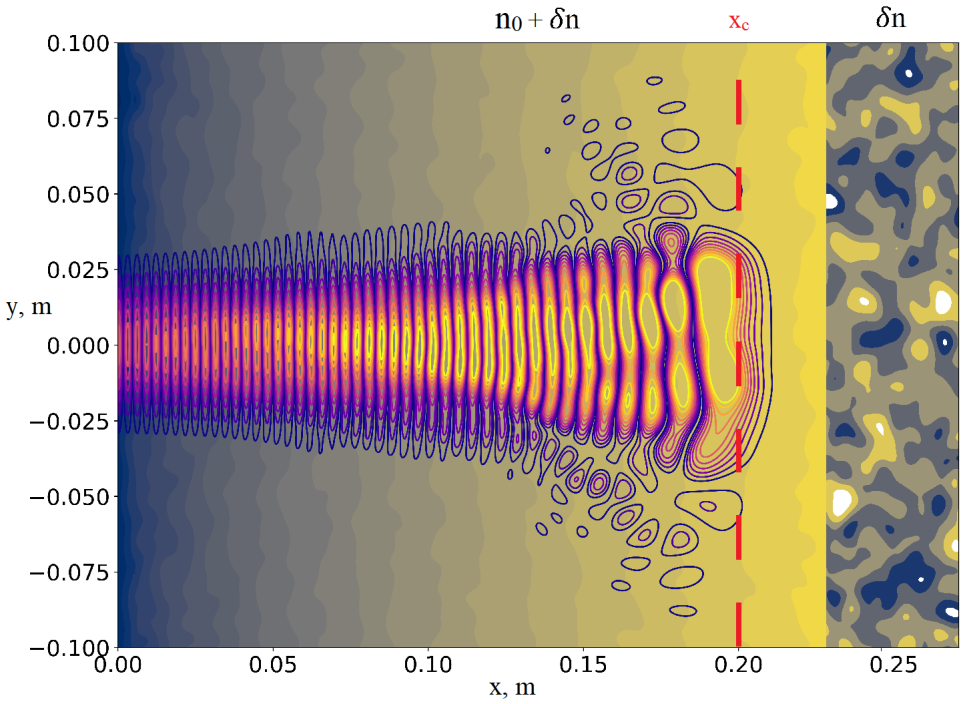

Figure 8. An example of the CUWA computation. The filled contours correspond to the full density profile $n_0 + \delta n$ (on the left, for $x < 0.225$ m) and its perturbation δn (on the right, for $x > 0.225$ m). The blue contour lines correspond to the electric field.

.

On the left side of the picture the background color corresponds to the total plasma density $n_0 + \delta n$, while the blue contour lines correspond to levels of constant magnitude of electric field. The red dashed line marks the position of the cut-off in the absence of density perturbations. Finally, on the right side of the image the density perturbations δn are presented for visualisation purpose.

To obtain the signal from the computation, a receiving antenna (coinciding with emitting one) was simulated by integrating the electric field along the grid boundary (corresponding to the antenna position) over the antenna pattern. The pattern in the

computation was chosen to be Gaussian (with a half-waist $\rho = 5$ cm, unless specified otherwise). To model conditions close to experimental ones [17], the central probing frequency was chosen to be 50 GHz and the cut-off was located at $L_0 = 10$cm.

3.2. Modelling results

A first computation was carried out under conditions as close to the theoretical 1D model (2.1) as possible by choosing a poloidal correlation length $l_{cy} = 20$ cm and $\rho = 10$ cm, making the turbulence essentially 1D. The radial correlation length l_{cx} was chosen to be 1 cm and ordinary polarization was utilized. The r.m.s. of delay times computed with CUWA are presented in Fig. 9.

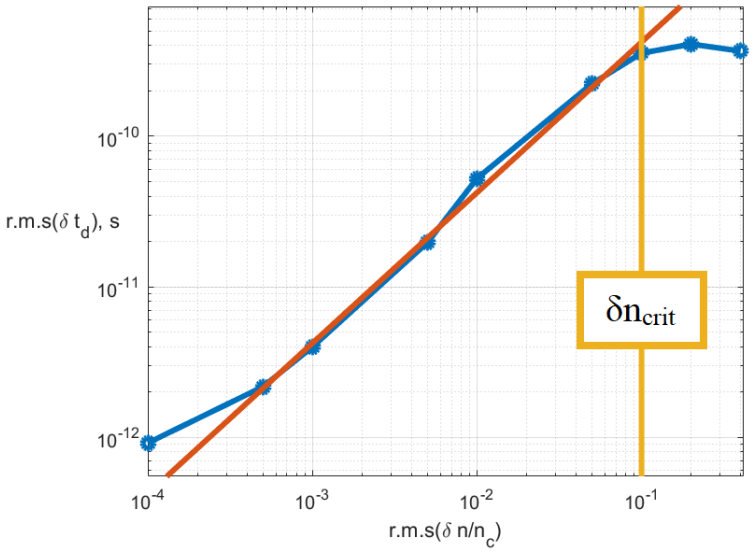

Figure 9. R.m.s of O-mode time delay vs the amplitude of the turbulence in the 1D limit. The blue curve corresponds to the full-wave computation, the red line is the prediction given by Eq. (17). The yellow line is the threshold amplitude given by (Eq. 6).

The first point (at the lowest fluctuation amplitude) corresponds to a delay r.m.s. much smaller than the period of the probing wave (2×10^{-11} s) and the numerical noise becomes too large to obtain reliable values of $\sqrt{\langle \delta t_d^2 \rangle}$. For the other points, the full-wave modelling results are in good ($\leq$15% of error in estimating turbulence amplitude) agreement with the prediction given by Eq. (17), which includes the correction factor of 2. This agreement implies that at least within the 1D limit our model produces relevant results. The main disagreement comes from the point $\delta n/n_c = 0.01$, where the computed delay r.m.s. turns out to be larger than the theoretical prediction. That in turn means that in that region the delay r.m.s. scales with turbulence amplitude at a higher power law than linear. That could be the case when the reflected pulse is strongly affected by nonlinear scattering effects, which are not included in our simplified model. Applying the criterion for strong non-linear scattering available for fluctuation reflectometry [27], for the given parameters we obtain $\delta n_{crit} = 0.013$, which is low enough to account for the observed discrepancy.

Nevertheless, nonlinear scattering effects unaccounted for in the model only seem to provide a relatively small deviation from the theoretical estimate for all the considered cases and will be considered in more detail in future work.

Another similar computation was carried out for X-mode polarization considering a linear density profile and $1/x$ profile for the magnetic field. The results are depicted in Fig. 10, also showing good agreement.

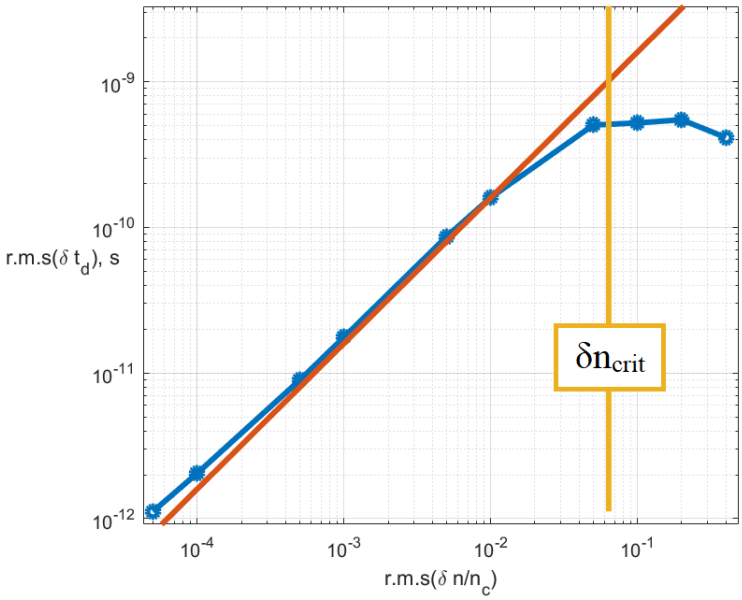

Figure 10. R.m.s of X-mode time delay vs the amplitude of the turbulence in the 1D limit. The blue curve corresponds to the full-wave computation, the red line is the prediction given by Eq. (15) multiplied by a factor of 2. The yellow line is the threshold amplitude given by Eq. 14.

Next a computation for more realistic parameters $l_{cx} = 1$ cm, $l_{cy} = 2$ cm and $\rho = 5$ cm was carried out. The results for O-mode are presented in Fig. 11.

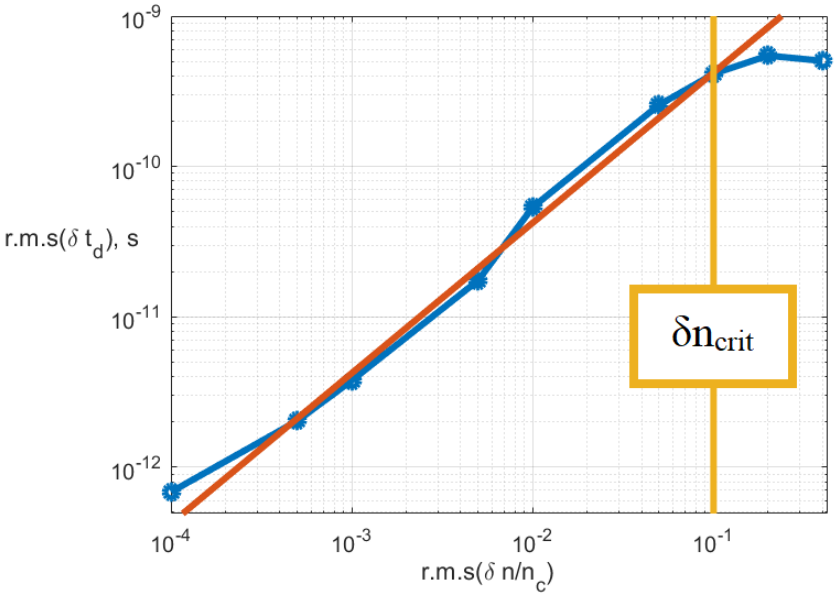

Figure 11. R.m.s of O-mode time delay vs the amplitude of the turbulence for realistic parameters. The blue curve corresponds to the full-wave computation, the red line is the prediction given by Eq. (17). The yellow line is the threshold amplitude given by Eq. (6).

Similar to the 1D case, within the relevant parameter range ($10^{-3} - 10^{-1}$), the analytical prediction is within 20% of the value obtained with CUWA. Unlike the previous cases, for some input amplitudes computed values turns out to be lower than the 1D expectation.

The likely explanation for this is that the density perturbations at small poloidal scale get "averaged out" across the finite waist of the probing beam. This makes the probing beam only sensitive to turbulence with poloidal scale comparable to ρ which means that for small values of l_{cy}/ρ only a limited part of the turbulence poloidal wavenumber spectrum provides contributions to the measurement, lowering the measured turbulence amplitude.

To test this explanation, a computation was done for the more extreme set of values $l_{cy} = 0.3$ cm and $\rho = 10$ cm. The resulting delay r.m.s. is expected to be significantly smaller than the one predicted by Eq. (17) and Fig. 12 indeed confirms this.

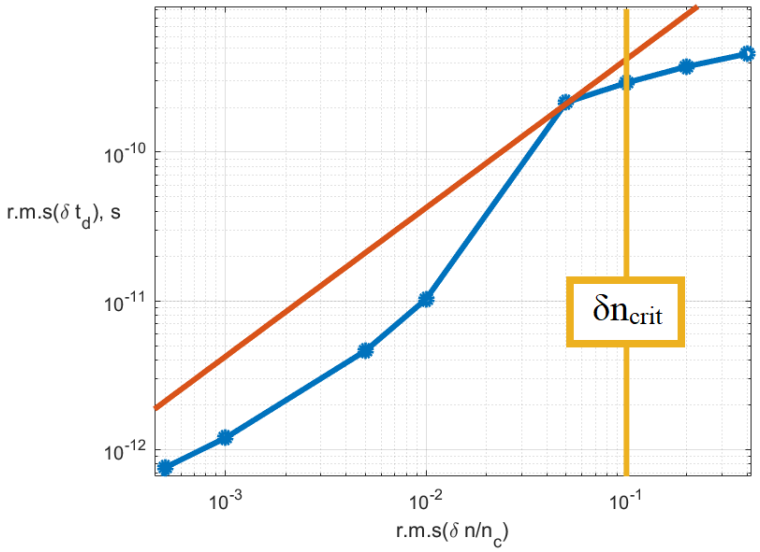

Figure 12. R.m.s of O-mode time delay vs the amplitude of the turbulence for large relative beam waist ρ/l_{cy}. The blue curve corresponds to the full-wave computation, the red line is the prediction given by Eq. (17). The yellow line is the threshold amplitude given by Eq. (6).

Finally, a CUWA computation for a set of probing frequencies and $l_{cx} = 1$ cm, $l_{cy} = 2$ cm and $\rho = 5$ cm was carried out to test the radial correlation length estimation method. A set of probing frequencies between 46 GHz and 54 GHz was used and the resulting CCF is plotted in Fig. 13.

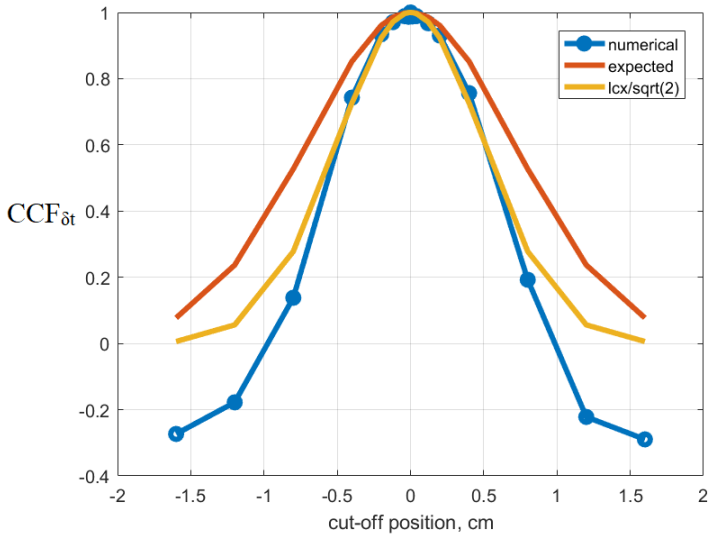

Figure 13. CCF of O-mode time delays vs the cut-off separation. The blue curve corresponds to the full-wave computation, the red line is the prediction given by Eq. (13). The yellow line is the same formula with l_{cy} divided by $\sqrt{2}$.

In the case of the radial correlation length measurement, the full-wave results entirely coincide with the 1D numerical integration. The turbulence amplitude used for this case was $5 \cdot 10^{-3} n_c$, i.e. the same value as in the previous section.

Overall, the results of the full-wave modelling are in good agreement with the expectation given by Eqs. (17) and (13), with the main sources of error being the finite beam sensitivity effects at small l_{cy}/ρ and nonlinear scattering effects at higher turbulence amplitudes. However, an error of nearly 20% in the estimation of the turbulence amplitude could be a significant factor when applied to experiment. Experimental application of the method would involve probing the plasma with a set of probing frequencies and obtaining both the radial correlation length of the turbulence and the profile of the turbulence amplitude over the covered radial range. An error of the order of 20% at each cut-off position could make it difficult to recover the qualitative shape of the turbulence amplitude profile.

Moreover, the numerical model used still possesses a number of simplifications: slab geometry, linear background density profile, uniform turbulence amplitude. Additional numerical modelling was therefore carried out to further explore the proposed turbulence profile measurement method and to address each of the model simplifications in turn. This will be discussed in the next section.

4. Model limitations

4.1. Turbulence profile measurement

Within this section, we will consider O-mode, but the result for X-mode is expected be qualitatively similar. CUWA modelling was carried out using a set of 19 probing

frequencies (with varying separation $\delta\omega$ between neighboring frequencies) in the range $f = [54 - 46]$ GHz. A set of 3000 random perturbation samples was used for each computation to preclude significant statistical errors.

The r.m.s. value of the resulting delay was computed for each probing frequency and the turbulence amplitude corresponding to each cut-off position was computed using Eq. (17). An example of all of the quantities is given in Fig. 14 to illustrate how the turbulence amplitude profile shape changes compared to the delay r.m.s. profile. It should be noted, that in Fig. 14c as well as other figures in this section the turbulence amplitude is normalized by a constant value $n_c(f_0)$, which means that the horizontal red line reflects a constant absolute value of density perturbation amplitude in space. The relative turbulence amplitude $\delta n/n_0$ is not constant and is increasing towards the plasma edge, as illustrated in Fig. 4.

This computation corresponds to the "default" case used in the previous section. The background density profile is linear and the turbulence amplitude is uniform across the computation domain. The slab geometry is used and the numerical parameters are:

f_0	$L_0(=x_c)$	ρ	l_{cx}	l_{cy}	$\frac{\sqrt{\langle\delta n^2\rangle}}{n_c(\omega_0)}$
50 GHz	10 cm	5 cm	1 cm	2 cm	$5\cdot10^{-3}$

Table 1. Default set of parameters used for the full-wave computations at multiple probing frequencies.

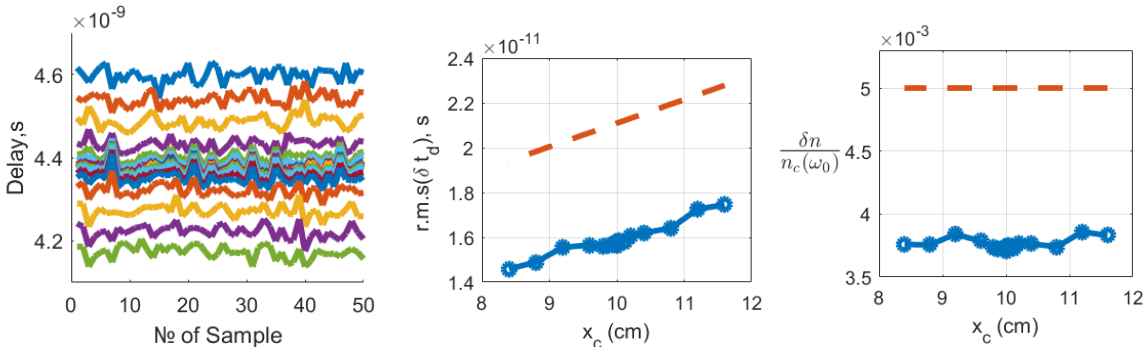

Figure 14. Example of data analysis process. (a) Delays computed for each turbulence sample (different colors correspond to different probing frequencies); (b) R.m.s. of delays computed for each probing frequency vs the cut-off radial position. The blue curve corresponds to the full-wave computation and the red dashed line is the prediction given by Eq. (17); (c) Turbulence amplitude profile. The blue curve corresponds to the full-wave computation data, the red dashed line corresponds to the constant turbulence amplitude profile used as an input for the full-wave computation.

Based on Fig. 11, one would expect the turbulence amplitude to be underestimated by about 20% for this value of input amplitude, which is indeed the case. Moreover, the 20% underestimation which we attribute to the beam sensitivity effect seems to be

a systematic shift, that does not affect the shape of the computed turbulence amplitude profile. To estimate the error specifically in the shape of the turbulence amplitude profile, computed δn values were multiplied by a constant factor to minimize the average error over all the probing frequencies. The maximum remaining error in this case is only 2.6%, suggesting that the error due to the 2D nature of the problem is consistent across all the probing frequencies and does not distort the shape of the measured profile.

To further confirm this idea additional computations were carried out for different input amplitudes of the turbulence. The resulting profiles are presented in Fig. 15, where for easier comparison they are normalized by the input turbulence amplitude $\frac{\delta n^{FW}(x)}{\delta n^{input}(x)}$.

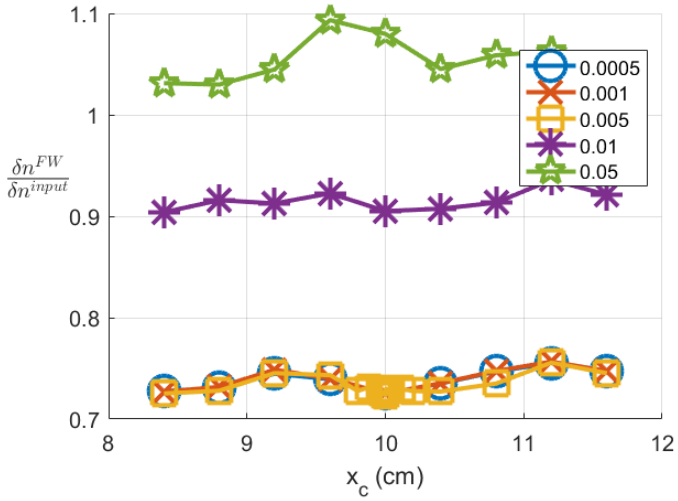

Figure 15. Turbulence amplitude profile normalised to input amplitudes. Different colors and markers correspond to different values of the relative input amplitude at the central cut-off.

Figure 15 is in agreement with our conclusions. For lower amplitudes, where nonlinear scattering is negligeble, the turbulence profile is consistent between different amplitudes, with a very small deviation from the input profile shape. For higher amplitudes, while the systematic error changes, the deviation from the input profile shape is still at most 3.6%, not affecting the profile shape significantly. Given the good consistency of the result for lower amplitudes and the high cost of simulations for multiple probing frequencies, in the rest of this section we will limit ourselves to considering the default input amplitude given in Table 1.

Next, we will test the profile reconstruction method against the other simplifications of the model using the "default" set of parameters given in Table 1 as the baseline and changing the parameters of interest.

4.2. Spatial dependencies

The first issue we address is to consider a nonlinear $n_0(x)$ profile instead of the linear one assumed in the model, as well as non-uniform turbulence amplitude over x.

In the case of nonlinear background density profile, the quantity L_0 corresponds to the *gradient scale length* of the profile. A full-wave computation was carried out for a parabolic density profile, which was selected to still have a $L_0 = 10$ cm gradient scale length at the central cut-off position:

$$n_0(x) = \left[1.25 - \frac{(1.5L_0 - x)^2}{L_0^2}\right] n_c(\omega_0), \tag{19}$$

In the region where Eq. (19) is negative, $n_0 = 0$ was assumed in CUWA. The amplitude of fluctuations was assumed to be uniform in space, resulting in a high relative turbulence amplitude at the plasma edge. The modelling results for this case are shown in Fig. 16.

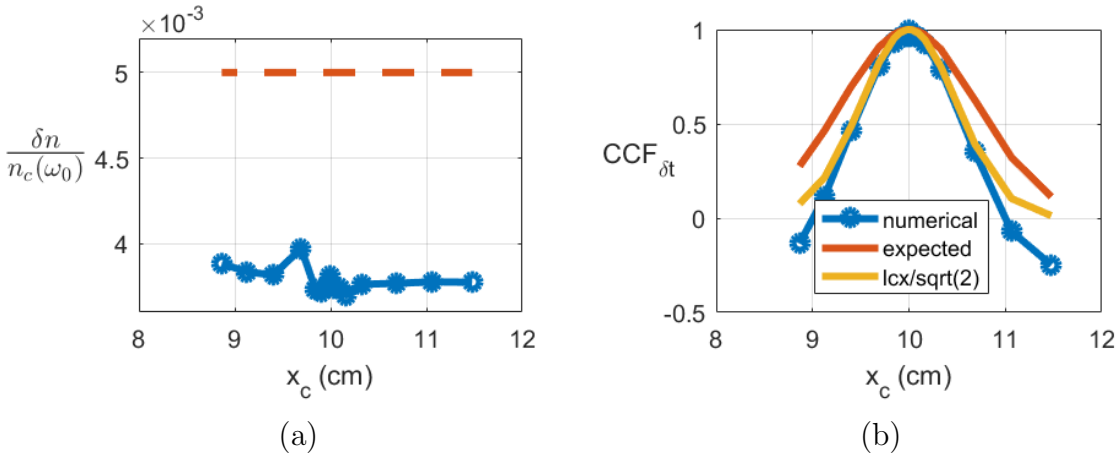

Figure 16. Quadratic $n_0(x)$ profile case. (a) Turbulence amplitude profile computed according to Eq. (17) with input l_{cx} value. The blue curve corresponds to the full-wave computation data, the red dashed line corresponds to the turbulence amplitude profile used as input. (b) Delay CCF function. The blue curve corresponds to the full-wave computation, the red curve corresponds to the input Gaussian turbulence CCF and the yellow curve corresponds to the same dependence with l_{cx} divided by $\sqrt{2}$.

In agreement with theoretical expectations, using a non-linear n_0 profile does not have a significant effect on the turbulence amplitude measurements. While the error between the "measured" and input turbulence amplitude is as high as 25%, the obtained dependence is only 4.8% different from the expected constant value.

Next, we reverted back to a linear n_0 profile and tested the influence of a non-uniform turbulence amplitude. As illustrated by Fig. 4, in all of the previous computations the relative amplitude of the turbulence had significantly increased towards the plasma edge without affecting the method. Significantly, this is not the case for conventional fast-sweeping reflectometry [28], in which a strong influence of edge turbulence on the measurements was found.

However, the variation of the turbulence amplitude in the covered radial range has so far been insignificant (around 15%) which is what we are addressing in this computation. The samples for this case were generated according to Eq. (18) and then multiplied by a factor $\exp(1 - \frac{x}{L_0})$. This resulted in the turbulence amplitude varying by about 40% along the scanned radial range and edge turbulence having the relative amplitude of up to . The computation for this case is given in Fig. 17:

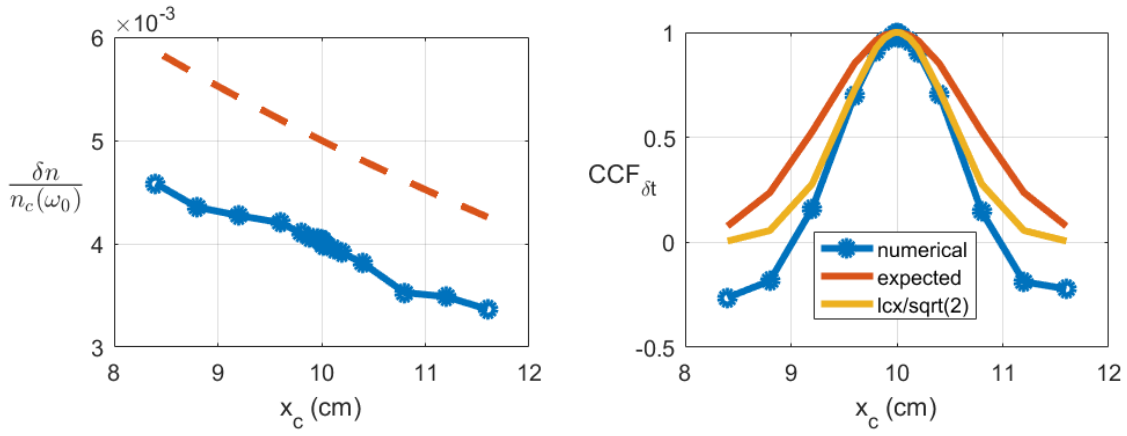

Figure 17. Exponential $\delta n(x)$ amplitude profile case. (a) Turbulence amplitude profile computed according to Eq. (17). The blue curve corresponds to the full-wave computation data, the red dashed line corresponds to the turbulence amplitude profile used as input. (b) Delay CCF function. The blue curve corresponds to the full-wave computation, the red curve corresponds to the input Gaussian turbulence CCF and the yellow curve corresponds to the same dependence with l_{cx} divided by $\sqrt{2}$.

Once again, the error in the shape of the measured profile turns out to be low (2.4%), suggesting that neither large edge turbulence nor the variation of the turbulence amplitude on the vicinity of the cut-off are a significant issue when estimating the pulse delay r.m.s. The possible explanation for this is the fact that SPR operates in the temporal domain and the edge turbulence scattering is naturally eliminated from the considered signal as it reaches the antenna at earlier times compared to the reflected pulse.

4.3. Geometrical factors

Next, the influence of 2D effects, not accounted for in the model, was studied. First of all, a computation was carried out with the default parameters (Table 1) except for $l_{cy} = 20$. Given the similarity to the near 1D computation presented in the previous section, we could expect the delay r.m.s. to increase and become closer to the prediction given by Eq. (17). The result of the profile reconstruction for this case is given in Fig. 18.

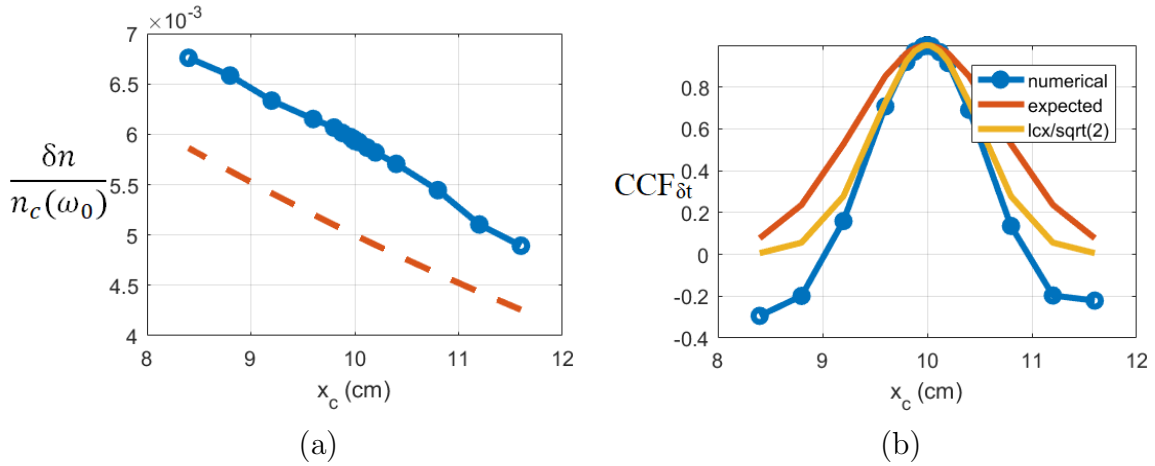

Figure 18. 1D δn case. (a) Turbulence amplitude profile computed according to Eq. (17). The blue curve corresponds to the full-wave computation data, the red dashed line corresponds to the turbulence amplitude profile used as input. (b) Delay CCF function. The blue curve corresponds to the full-wave computation, the red curve corresponds to the input Gaussian turbulence CCF and the yellow curve corresponds to the same dependence with l_{cx} divided by $\sqrt{2}$.

In agreement with our expectations, the delay r.m.s. increases, while the shape is still reproduced (within a relative error of 2%). The results presented in Fig. 18 suggest that the 2D effects of the turbulence result in a consistent systematic decrease in the density amplitude measurement and that the turbulence profile can still be measured. The fact that the delay r.m.s. in this case actually became larger than the analytical expectation is puzzling, especially when compared to Fig. 9. It could be related to the different number of samples or different values of ρ associated with the two figures. Since the difference in delay r.m.s. lies within the 20% error observed in the previous section, we will not explore it further in this work.

Another geometrical limitation is the use of slab geometry. In a realistic scenario, the magnetic surfaces of the plasma have curvature, which could influence the propagation of the beam. To test how the curvature of the background density profile affects the pulse delay, a computation was carried out with the following background density profile:

$$n_0(x,y) = \begin{cases} \dfrac{R - \sqrt{(x-R)^2 + y^2}}{L_0} n_c(\omega_0) & \text{for } \sqrt{(x-R)^2+y^2} \leq R, \\ 0 & \text{for } \sqrt{(x-R)^2+y^2} > R. \end{cases} \tag{20}$$

The density fluctuations were also adapted to follow the curvature of the background profile, with l_{cy} becoming the correlation length along the circular surface of constant n_0. This was done by generating $\delta n(x', y')$ according to Eq. (18) and then remapping it to (x, y) following the rule:

$$(x,y) = \left(R - (R-x') \cdot \cos\left(\frac{y'}{R-x'}\right), (R-x') \cdot \sin\left(\frac{y'}{R-x'}\right) \right). \tag{21}$$

For the computation, default parameters were used and R was chosen to be 25 cm. Computation results are given in Fig. 19.

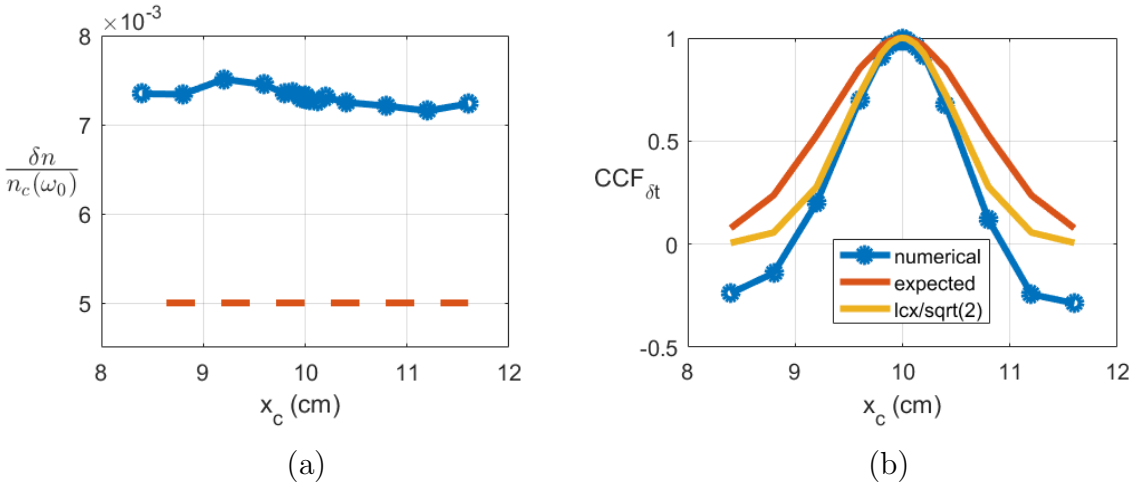

Figure 19. Finite plasma curvature case. (a) Turbulence amplitude profile computed according to Eq. (17). The blue curve corresponds to the full-wave computation data, the red dashed line corresponds to the turbulence amplitude profile used as input. (b) Delay CCF function. The blue curve corresponds to the full-wave computation, the red curve corresponds to the input Gaussian turbulence CCF and the yellow curve corresponds to the same dependence with l_{cx} divided by $\sqrt{2}$.

While the relative error in the profile is still low (less than 3%), the average value of the delay r.m.s. in higher this case. A possible explanation could be the fact that due to the curvature of the cut-off, only the central portion of the reflected beam will reach the antenna. This effectively increases the beam sensitivity to turbulence with smaller poloidal scales and results in a higher delay r.m.s. as shown in the previous section. This result is consistent with the one obtained for conventional fluctuation reflectometry [29], where full-wave computations showed an increase of measured turbulence amplitude at higher curvature. To test this explanation, a set of full-wave simulations were carried out with the same parameters except for $l_{cy} = 20$ cm, for $R = 25$ cm and $R = 100$ m (slab limit). The reconstructed profiles are presented in Fig. 20.

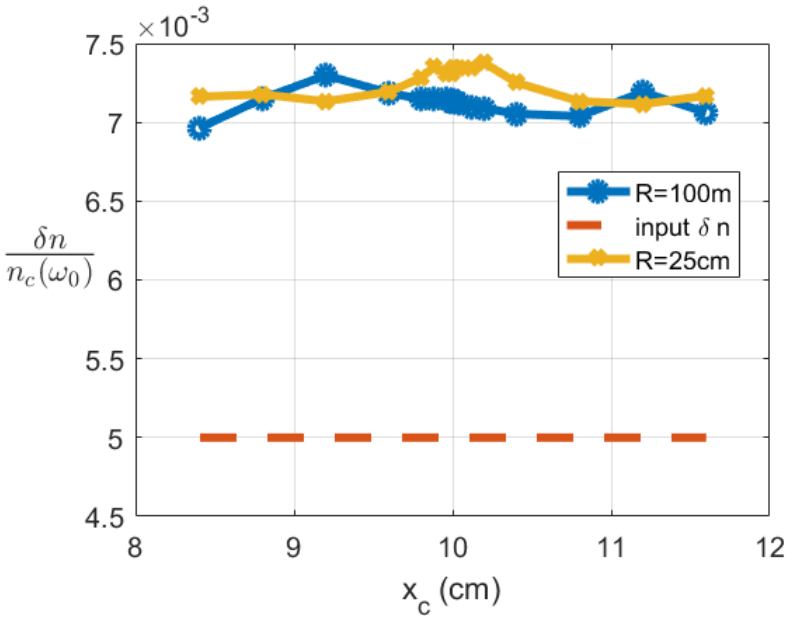

Figure 20. Turbulence amplitude profile computed according to Eq. (17). The blue and yellow curves correspond to the full-wave computation data considering $l_{cy} = 20$ cm as well as $R = 100$ m and $R = 25$ cm respectively, the red dashed line corresponds to the profile used as input for the full-wave computation.

Such a long poloidal correlation length was used to exclude the $l_{cy}/\rho < 1$ effect, and assuming it was the cause for the large delay r.m.s., there should be no difference between the two computations. That is indeed the case as the two computations provide results within 4% of each other.

Overall, the computations presented in this section confirm that additional effects, while introducing a systematic error in to the absolute value of the turbulence amplitude, do not significantly affect the estimation of the turbulence amplitude profile shape. Moreover, the delay CCF does not appear sensitive to any of the considered effects.

5. Discussion

Summarizing the computation results obtained in the previous sections, we conclude that the proposed method provides information about the shape of the radial profile of the turbulence amplitude and its radial correlation length.

However, the absolute value of the measured turbulence amplitude is strongly affected by the curvature of the plasma and the poloidal correlation length of the turbulence (with respect to the waist of the probing beam) and potential nonlinear scattering effects. To compare the absolute values of the turbulence amplitude between different discharges, one therefore has to ensure that the geometry and the turbulence poloidal scale are similar.

The modelling presented in Sec. 4, as well as additional modelling done within this work, shows a consistent monotonic increase of delay r.m.s. with both stronger plasma curvature and longer l_{cy}. Both of these effects seem to be caused by finite sensitivity of

the beam, making the ratio of poloidal scale of the turbulence to the effective beam size a key parameter to consider. Further improvements of the method to account for this effect are possible and will be a subject of future work.

When compared to conventional fluctuation reflectometry and FSR methods, the new technique seems to be affected by nonlinear scattering effects and beam sensitivity in a similar manner. At the same time the competitive benefit of the method seems to lie in utilizing the temporal domain and excluding the influence of the strong edge turbulence on the measurements. Overall it appears that SPR delay analysis is a more capable analog for the turbulence measurements carried out with continuous operation.

At the same time, the correlation technique applied within the method has proven to be robust and to provide a correct estimate of the turbulence radial correlation length l_{cx}, regardless of the probing geometry.

The natural point of comparison for this part of the method is the RCR diagnostic, which utilizes a similar approach to measure l_{cx}. Measurements with this diagnostic tend to overestimate l_{cx} in the linear scattering regime [4, 30]. At the same time, in the strongly nonlinear regime, the measured correlation length does not directly correspond to l_{cx} [31] and tends to be lower than l_{cx} in experimental measurements [32]. We may ask whether the proposed SPR method suffers from the same disadvantages as classic RCR. To answer this question, two more computations were carried out using the default parameters (Table 1) and different relative amplitudes of the turbulence. The CCFs obtained in these cases are given in Fig. 21.

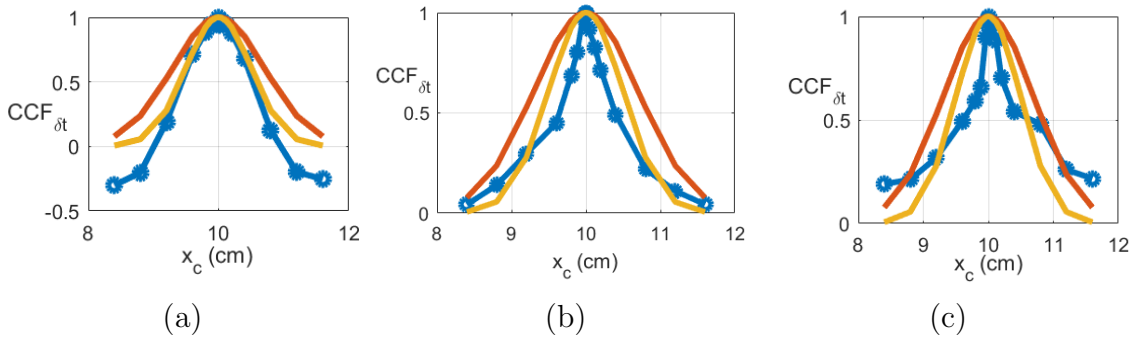

Figure 21. Delay CCF function for relative turbulence amplitude $\delta n/n_c(\omega_0)$ (a) 0.0017, (b) 0.058 and (c) 0.13. The Blue curves correspond to the full-wave computation, the red curves correspond to the input Gaussian turbulence CCF and the yellow curves correspond to the Gaussian dependence with l_{cx} divided by $\sqrt{2}$.

Specific values of the amplitude selected do not have particular meaning and were selected arbitrarily due to different amplitude normalization used in the code.

The criterion for the onset of the nonlinear regime [31], applied to the default computation parameters, gives us a turbulence level threshold $\frac{\delta n_{crit}}{n_c} = 0.013$, suggesting that the results presented in the previous section with $\delta n/n_c(\omega_0) = 5 \cdot 10^{-3}$ lie within the linear scattering regime limit. According to this value, Fig.21a corresponds to a linear scattering regime, while Figs.21b, c describe the strongly nonlinear scattering regime. At the same time only Fig.21c reaches the amplitude threshold Eq.(6) within our model.

From Figures 21a-c, one can see that the computed CCF remains in agreement with the expectations within the limits of the linear scattering case, but in the nonlinear regime we see the narrowing that is expected from the RCR technique, even before the critical density estimate given by Eq.(6) is reached. A more detailed comparison of the two threshold values is also a subject of future studies.

It appears, however, that linear broadening [4] does not occur within the proposed method, making it superior to classic RCR. Additionally, in the case of SPR, probing with the entire set of probing frequencies can be performed within the same discharge [16], making correlation measurements easier to implement.

An additional capability of the SPR could lie in the temporal analysis the pulse delays. Since we attribute the perturbation of delay to the perturbation of the cut-off, the frequency spectrum of t_d should correspond to the frequency spectrum of the turbulence.

However, within this paper we are not accounting for the temporal evolution of the turbulence generating independent samples instead. This will be the subject of future work, where a realistic turbulence generated with the help of gyrokinetic modelling will be used.

One more point to discuss are the empirical numerical coefficients introduced in Sec. 2.2. Given the consistent behavior between different polarizations, they are likely associated with the step-like density perturbation employed within the model. These coefficients could have different values if a more realistic turbulence spectrum was considered. To fully justify them, a set of computations for different realistic spectra, similar to [26], is needed. Such work is currently underway employing gyrokinetic modelling to produce a realistic turbulence spectrum.

Nevertheless, in the case of the turbulence amplitude profile measurement, any change in the numerical factor would likely only add to the systematic error without affecting the measured profile shape, preserving the viability of the method for studying the turbulence amplitude profile. While the estimate of radial correlation length l_{cx} might be affected by an error in the numerical coefficient, it is still expected to provide a value of the correct order of magnitude to use in Eq. (17).

Finally, from an experimental standpoint, one can conclude that the reduced model does not have any significant applicability limitations, provided the absolute values of the turbulence amplitude obtained with the method are compared for similar geometries and turbulence conditions. The main limiting factor for experimental application is the possible presence of multiple cut-offs, appearing for turbulence amplitudes higher than the critical value given by Eq. (6). Unfortunately, to determine whether the measurement is done in that regime one has to have prior knowledge of the turbulence amplitude and of its radial correlation length. However, due to the strong drop-off of the correlation in the nonlinear case (Figs.21c), the radial correlation length in the nonlinear regime will be underestimated, resulting in a lower threshold value given by Eq. (6) Satisfying this threshold will at least guarantee that the unfavorable multiple cut-off case (Fig. 3) is not reached.

For example using Fig. 21b we would estimate l_{cx} as 0.7 cm, resulting in a threshold value of $\frac{\delta n}{n_c(\omega_0)} = 0.07$ rather than the correct value of 0.1. Satisfying this more restrictive threshold would guarantee that the turbulence amplitude profile measurement is not affected by multiple cut-offs, even if the radial correlation length measurements are affected by nonlinear effects.

Considering Eq. (6), the most favorable measurement regime corresponds to the case of either relatively low turbulence amplitude or relatively small gradient scale length, making the measurements deeper in the core potentially challenging, as the gradient scale length becomes large. At the same time, at the plasma edge turbulence amplitude is known to be large making it potentially higher than the threshold value.

In the case of X-mode probing, the amplitude threshold condition for X-mode given by Eq. (A.9) benefits from measurements at low densities, once again making the plasma edge a viable measurement location.

Summarizing, the SPR turbulence measurement is well-suited for the plasma edge, where the density gradient scale length is small. A possible exception to that is the top of the pedestal in H-mode, although it is difficult to predict whether the increase of the gradient scale length or the reduction of turbulence level will be a more significant factor.

In either case, in the data processing stage, each measurement should be compared against the threshold value to ensure its validity. An additional method of determining quality of the measurement based on its statistical properties is currently being developed.

Aside from the specifics of microwave propagation in plasma, a potential experimental concern is the perturbation of the pulse shape and delay in the transmission lines leading up to the plasma. Indeed, the uncertainty in the measurements becoming comparable to the r.m.s. of the delay related to the turbulence would pose a significant problem for the proposed method. However, in the case of the TCV SPR system, even in the case of analog delay acquisition the measurement error of the pulse delay was found to be at most 40 ps with the typical r.m.s. of delay being 100 ps [17]. Moreover, in the case of digital acquisition currently employed in the TCV SPR, the error further decreases down to about 20 ps with the delay r.m.s. in the cases being considered so far being of the order of 200 ps, leading us to believe that with appropriate calibration experimental uncertainties do not pose a significant problem for the proposed method.

Conclusions

Within this paper, a new method for measuring the amplitude and radial correlation length of turbulence has been proposed using short pulse reflectometry. A simple theoretical model has been utilized to obtain analytical expressions for the turbulence amplitude based on the variation of the SPR pulse delays for both O and X polarizations of the probing wave. Within the same model, an application of the correlation technique to the SPR delay has been demonstrated to provide information about the turbulence

radial correlation length.

Analytical predictions have then been validated with 2D full-wave simulations, which have been employed both to confirm the feasibility of the proposed method and to explore its limitations connected to experimental effects not accounted for in the theoretical model. The robustness of the method has been demonstrated and the limits of applicability to experiment outlined.

Acknowledgments

The full-wave numerical simulations have been carried out on the EUROfusion High Performance Computer (Marconi- Fusion).

Appendix A. X-mode polarization

To derive the delay r.m.s. in the case of X polarization of the probing wave, we will utilize the X-mode dispersion relation.

$$k^2 = \frac{1}{c^2}\frac{\left(\omega^2 - \omega_{ce}\omega - \omega_{pe}^2\right)\left(\omega^2 + \omega_{ce}\omega - \omega_{pe}^2\right)}{\omega^2 - \omega_{ce}^2 - \omega_{pe}^2}, \tag{A.1}$$

here, $\omega_{ce} = \frac{eB}{m_e c}$ is the electron cyclotron frequency and $\omega_{pe} = \frac{4\pi n e^2}{m_e}$ is the plasma frequency.

Using Eq. (A.1), we can obtain an estimate for the inverse group velocity:

$$\frac{1}{v_g} = \frac{\partial k}{\partial \omega} = \frac{\omega}{kc^2}\frac{\left(\omega^2 - \omega_{ce}^2 - \omega_{pe}^2\right)^2 + \omega_{pe}^2\omega_{ce}^2}{(\omega^2 - \omega_{ce}^2 - \omega_{pe}^2)^2}. \tag{A.2}$$

At the cut-off, this quantity goes to infinity (due to a vanishing k), as for the ordinary mode. Since we are mainly considering the effect a density perturbation at the cut-off has on the delay time, we can ignore the rest of the integral in Eq. (1):

$$t_d = 2\int_0^{x_c}\frac{dx}{v_g} = \overbrace{2\int_0^{x_c - l_{cx}}\frac{\partial k}{\partial \omega}dx}^{\text{unperturbed } T_0} + \overbrace{2\int_{x_c - l_{cx}}^{x_c + \delta x_c}\frac{\partial k}{\partial \omega}dx}^{\text{perturbed } T_1}; \tag{A.3}$$

In the perturbed term, we will assume that all background factors vary slowly within l_{cx} of the cut-off and move them outside the integral:

$$T_1 \approx \frac{2h(x_c)}{c}\int_{x_c - l_{cx}}^{x_c + \delta x_c}\frac{\sqrt{\omega}dx}{\sqrt{\omega - \frac{1}{2}\left[\omega_{ce}(x) + \sqrt{\omega_{ce}^2(x) + 4\omega_{pe}^2(x)}\right]}}; \tag{A.4}$$

$$h(x) = \sqrt{\omega}\frac{\left(\omega^2 - \omega_{ce}^2 - \omega_{pe}^2\right)^2 + \omega_{pe}^2\omega_{ce}^2}{(\omega^2 - \omega_{ce}^2 - \omega_{pe}^2)^{3/2}\sqrt{\left[\omega^2 + \omega_{ce}\omega - \omega_{pe}^2\right]\left[\omega - \frac{1}{2}(\omega_{ce} - \sqrt{\omega_{ce}^2 + 4\omega_{pe}^2})\right]}}. \tag{A.5}$$

Here, we have assumed that the upper cut-off $\omega_U = \frac{1}{2}(\omega_{ce} + \sqrt{\omega_{ce}^2 + 4\omega_{pe}^2})$ is the one that the probing wave reflects at, which is typical for reflectometry experiments. To estimate the integral over x we will use a linear approximation to describe the spatial dependence of the magnetic field and density:

$$\frac{1}{L_c} = \frac{\frac{\partial \omega_U}{\partial x}}{\omega} = \underbrace{\frac{1}{B}\frac{\partial B}{\partial x}}_{1/L_B} \frac{\omega_{ce}}{2\omega}\left(1 + \frac{1}{\sqrt{1 + \frac{4\omega_{pe}^2}{\omega_{ce}^2}}}\right) + \underbrace{\frac{1}{n}\frac{\partial n}{\partial x}}_{1/L_n} \frac{\omega_{pe}}{2\omega\sqrt{1 + \frac{\omega_{ce}^2}{4\omega_{pe}^2}}}. \tag{A.6}$$

Assuming that the amplitude of density perturbations is small, we can estimate the shift of the cut-off surface. We will use designations ω_U, ω_{pe} and x_c for unperturbed quantities. In that case, the shift of the cut-off can be estimated in the following way:

$$\omega = \omega_U(x_c + \delta x_c) + \delta\omega_U(x_c + \delta x_c) \approx \omega + \omega\frac{\delta x_c}{L_c} + \frac{\delta n}{2n_0(x)}\frac{\omega_{pe}}{\sqrt{1 + \frac{\omega_{ce}^2}{4\omega_{pe}^2}}}, \tag{A.7}$$

$$\delta x_c = -L_c\frac{\delta n}{2n_0(x)}\frac{\omega_{pe}}{\omega\sqrt{1 + \frac{\omega_{ce}^2}{4\omega_{pe}^2}}}. \tag{A.8}$$

Similarly to Eq. (3), we can use this formula to find the critical density, limiting the application of our approach:

$$\frac{\delta n_{crit}}{n_0(x_c)} = 2\frac{l_{cx}}{L_c}\frac{\omega}{\omega_{pe}}\sqrt{1 + \frac{\omega_{ce}^2}{4\omega_{pe}^2}}. \tag{A.9}$$

Now that we have obtained the expression for the cut-off shift, we can integrate Eq. (A.4).

$$\begin{aligned} T_1 &\approx \frac{2h(x_c)}{c}2\sqrt{L_c}\sqrt{l_{cx} - L_c\frac{\delta n}{2n_0(x)}\frac{\omega_{pe}}{\omega\sqrt{1 + \frac{\omega_{ce}^2}{4\omega_{pe}^2}}}} \\ &\approx \frac{2h(x_c)}{c}2\sqrt{L_c l_{cx}} - \frac{L_c}{c}\sqrt{\frac{L_c}{l_{cx}}}h(x_c)\frac{\delta n}{n_0(x)}\frac{\omega_{pe}}{\omega\sqrt{1 + \frac{\omega_{ce}^2}{4\omega_{pe}^2}}}. \end{aligned} \tag{A.10}$$

Finally, we can arrive at the expression for the delay r.m.s.

$$\sqrt{\langle(t_d - \langle t_d\rangle)^2\rangle} = \frac{L_c}{c}\sqrt{\frac{L_c}{l_{cx}}}h(x_c)\frac{\sqrt{\langle\delta n^2\rangle}}{n_0(x)}\frac{\omega_{pe}}{\omega\sqrt{1 + \frac{\omega_{ce}^2}{4\omega_{pe}^2}}}. \tag{A.11}$$

References

[1] H J Hartfuss, T Geist, and M Hirsch. In: *Plasma Phys. Control. Fusion* 39.11 (1997), p. 1693.

[2] E Mazzucato. In: *Review of Scientific Instruments* 69.6 (1998), pp. 2201–2217.

[3] R Nazikian, G J Kramer, and E Valeo. In: *Physics of Plasmas* 8.5 (2001), pp. 1840–1855.

[4] I H Hutchinson. In: *Plasma Physics and Controlled Fusion* 34.7 (1992), pp. 1225–1251.

[5] E Mazzucato and R Nazikian. In: *Phys. Rev. Lett.* 71 (12 1993), pp. 1840–1843.

[6] L Vermare et al. In: *Nuclear Fusion* 46.9 (2006), S743–S759.

[7] A Medvedeva et al. In: *Plasma Physics and Controlled Fusion* 59.12 (2017), p. 125014.

[8] G D Conway et al. In: *Plasma Physics and Controlled Fusion* 47 (2005), p. 1165.

[9] J Schirmer et al. In: *Plasma Physics and Controlled Fusion* 49.7 (2007), pp. 1019–1039.

[10] V F Shevchenko, A A Petrov, and V G Petrov. In: *International Journal of Infrared and Millimeter Waves* 14 (1993), pp. 1755–1768.

[11] C W Domier, Y Roh, and N C Luhmann Jr. In: *Review of Scientific Instruments* 70 (1999), p. 1038.

[12] C W Domier, Y Zhu, and N C Luhmann Jr. In: *Review of Scientific Instruments* 92 (2021), p. 034714.

[13] T Tokuzawa et al. In: *Review of Scientific Instruments* 74 (2003), p. 1506.

[14] B I Cohen, T B Kaiser, and J C Garrison. In: *Review of Scientific Instruments* 68 (1997), p. 1238.

[15] B I Cohen et al. In: *Physics of Plasmas* 6 (1999), p. 1732.

[16] P A Molina Cabrera et al. In: *Review of Scientific Instruments* 90.12 (2019), p. 123501.

[17] P A Molina Cabrera et al. In: *Plasma Physics and Controlled Fusion* 63.8 (2021), p. 085019.

[18] O Krutkin et al. In: *Plasma Physics and Controlled Fusion* 65.1 (2022), p. 015013.

[19] P Aleynikov and N B Marushchenko. In: *Computer Physics Communications* 241 (2019), pp. 40–47.

[20] V L Ginzburg. *The propagation of electromagnetic waves in plasmas*. Oxford, Pergamon, 1964.

[21] E Z Gusakov and N V Kosolapova. In: *Plasma Physics and Controlled Fusion* 53.4 (2011), p. 045012.

[22] E Z Gusakov and O L Krutkin. In: *Plasma Physics Reports* 43.6 (2017), pp. 605–613.

[23] E Z Gusakov, M A Irzak, and A Yu Popov. In: *Plasma Physics and Controlled Fusion* 56.2 (2014), p. 025009.

[24] O L Krutkin et al. In: *Plasma Physics and Controlled Fusion* 62.4 (2019), p. 045010.

[25] J R Pinzón et al. In: *Plasma Physics and Controlled Fusion* 59.3 (2017), p. 035005.

[26] J Ruiz Ruiz et al. In: *Plasma Physics and Controlled Fusion* 64.5 (2022), p. 055019.

[27] E Z Gusakov and A Yu Popov. In: *Plasma Physics and Controlled Fusion* 44 (2002), p. 2327.

[28] G V Zadvitskiy et al. In: *Plasma Physics and Controlled Fusion* 60.2 (2018), p. 025025.

[29] J. Vicente et al. In: *Plasma Physics and Controlled Fusion* 62 (2020), p. 025031.

[30] E Z Gusakov and B O Yakovlev. In: *Plasma Physics and Controlled Fusion* 44.12 (2002), pp. 2525–2537.

[31] E Z Gusakov and A Yu Popov. In: *Plasma Physics and Controlled Fusion* 46.9 (2004), pp. 1393–1408.

[32] O L Krutkin et al. In: *Nuclear Fusion* 59.9 (2019), p. 096017.